Two-dimensional profiling of carriers in a buried heterostructure multi-quantum-well laser: Calibrated scanning spreading resistance microscopy and scanning capacitance microscopy

D. Ban and E. H. Sargent
Edward S. Rogers Sr. Department of Electrical and Computer Engineering, 10 King's College Road, Toronto, Ontario M5S 3G4, Canada

St. J. Dixon-Warren,[a)] T. Grevatt, G. Knight, G. Pakulski, A. J. SpringThorpe, R. Streater, and J. K. White
Nortel Networks, Optical Components, 3500 Carling Avenue, Ottawa, Ontario K2H 8E9, Canada

(Received 20 November 2001; accepted 12 August 2002)

We report results of a scanning spreading resistance microscopy (SSRM) and scanning capacitance microscopy (SCM) study of the distribution of charge carriers inside multi-quantum-well (MQW) buried heterostructure (BH) lasers. We demonstrate that individual quantum-well–barrier layers can be resolved using high-resolution SSRM. Calibrated SSRM and SCM measurements were performed on the MQW BH laser structure, by utilizing known InP dopant staircase samples to calibrate the instrumentation. Doping concentrations derived from SSRM and SCM measurements were compared with the nominal values of both *p*- and *n*-doped regions in the MQW BH lasers. For *n*-type materials, the accuracy was bias dependent with SSRM, while for SCM, excellent quantitative agreement between measured and nominal dopant values was obtained. The SSRM was able to measure the dopant concentration in the *p*-type materials with ~30% accuracy, but quantitative measurements could not be obtained with the SCM. Our results demonstrate the utility of combining calibrated SSRM and SCM to delineate quantitatively the transverse cross-sectional structure of complex two-dimensional devices such as MQW BH lasers, in which traditional one-dimensional probing using secondary ion mass spectroscopy provides only a partial picture of internal device structure. © *2002 American Vacuum Society.* [DOI: 10.1116/1.1511211]

I. INTRODUCTION

Buried heterostructure (BH) multi-quantum-well (MQW) lasers[1–5] provide tight confinement of charge carriers and photons within the device active region as defined by a lateral current-blocking structure. BH MQW lasers exhibit low-threshold currents, high efficiencies and stable, circular transverse far-field profiles. The distribution of dopants in the active and current-blocking regions of the BH MQW lasers plays a key role in determining device performance. Two-dimensional (2D) dopant profiling is, therefore, of great interest and demand in diagnosing and improving laser performance, due to the capability of directly clarifying the role of lateral current channeling and unintended leakage in BH lasers.

Two promising techniques for 2D imaging of optoelectronic devices in cross section are scanning spreading resistance microscopy (SSRM) (Refs. 6 and 7) and scanning capacitance microscopy (SCM).[8] SSRM and SCM,[9] both based on atomic force microscopy (AFM), employ a conductive tip in direct contact with the sample surface. These allow for semiquantitative measurement of the spatial free-carrier distribution of the optoelectronic device under test.

In SSRM mode, a dc bias voltage is applied to the tip and the resulting current through the sample is measured as a function of the tip position on the surface using a six-decade logarithmic amplifier. A simple analysis suggests that the current should be inversely proportional to the spreading resistance in the vicinity of the tip and is thus proportional to the product of the local free-carrier concentration (n) and the carrier mobility (μ) near the point contact. However, variations in the tip–surface contact resistance must also be considered.[10]

In SCM, an ultra-high-frequency (UHF) resonant capacitance sensor forms the basis of the capacitance detection. The resonator connects to the conductive probe tip via a transmission line. A sinusoidal bias is applied to the sample, driving the semiconductor surface at the point contact back and forth repetitively from accumulation to depletion. The alternating depletion and accumulation of carriers under the tip gives rise to variation in the capacitance of the tip–sample junction. This change in capacitance is detected by a shift in the center frequency or phase of the resonance circuit that includes the sensor, the transmission line, probe, and semiconductor sample. The SCM dC/dV signal is acquired as the tip scans over the semiconductor surface. The magnitude of the SCM signal is related to the local carrier concentration in the sample.

During the early stage of the development of these two techniques, most of the attention was focused on silicon-based structures and devices,[11–15] including *pn*-junction delineation or semiquantitative imaging of the doped regions in electronic devices such as metal–oxide–semiconductor

[a)]Author to whom correspondence should be addressed; electronic mail: stj.dixon.warren@utoronto.ca

field-effect transistors. More recently, there have been a number of reports concerning InP structures.[16–18] SSRM has been used to determine the dopant profiles in various semiconductor structures with spatial resolution on the order of the tip radius (20 nm). Quantitative determination of dopant levels is also possible by using suitable standard samples for calibration.[10]

In the present work, we report calibrated SSRM and SCM measurements on BH MQW lasers. We show that individual quantum wells in the laser active region may be resolved. Junctions between *p*- and *n*-doped regions are clearly observable in both SSRM and SCM images. Carrier concentrations as derived from SSRM and SCM measurements are compared to secondary ion mass spectroscopy (SIMS) results on both *p*- and *n*-doped regions in the structures. The bias dependence of the SSRM and SCM measurements is investigated and discussed.

II. EXPERIMENT

Our SSRM and SCM experiments are conducted on a commercial atomic force microscope system (Digital Instruments Nanoscope III AFM with a Dimension 3100 head). In view of previously reported results on III–V compound semiconductor samples,[18] we used commercially available boron-doped diamond-coated cantilever tips (Digital Instruments, spring constant = 40 N/m) in our measurements for quantitative correlation between the SSRM and SCM measurements and SIMS results.

The SSRM option implements a sensitive six-decade (1 mA–1 nA) logarithmic amplifier to measure the electric current flowing from the tip through the sample and to the sample chuck as a function of the AFM tip position. The SSRM measurements were performed under contact-mode AFM feedback conditions. The tip was scanned at 0.25–4 μm/s with forces in the range of 2–5 μN. The sample bias voltage was varied from +0.5 to 3.5 V dc.

Four parameters define the SCM operating point: the ac bias modulation voltage, the modulation frequency, the dc offset voltage, and the capacitor sensor probing voltage. A dc offset voltage is used to compensate the $C-V$ curve flatband shift caused by charge trapped in the dielectric layer and Fermi-level variation. In practice, this dc voltage is adjusted to maximize the change in differential capacitance signal (maximum $C-V$ curve slope). Data were acquired in two different SCM modes: (i) "dC/dV," in which either the amplitude or phase of the capacitance variation is obtained for a given voltage modulation on the sample; and (ii) "feedback," wherein the ac voltage is adjusted to maintain a constant capacitance (depletion depth) throughout the image. As with SSRM, the tips were scanned in contact mode at 0.25–4 μm/s but with a much lower contact force. The sample bias voltage was varied from 0.2 to 1.5 V ac.

The strained-layer multiple-quantum-well active region structure of the BH MQW lasers used for these SSRM and SCM measurements was grown by metal organic chemical vapor deposition (MOCVD) method. The mesa of the BH laser was buried by a four-layer thyristor structure with alternating doping type (*n*- or *p*-doped) and concentration. Five quantum wells were separated by barrier layers. The BH laser samples were metallized with ohmic contacts. The epitaxial InP structures with staircase doping profiles were grown by molecular beam epitaxy (MBE) on epiready wafers. The doping concentration varied from 10^{16} to 10^{19} cm^{-3} for both *n*-type Si and *p*-type Be-doped staircase structures. The wafers were cleaved to expose the cross section of interest for SSRM and SCM measurements. Liquid InGa alloy was applied to the back surfaces of the MBE calibration samples for electrical contacting. The samples were then mounted with the cleaved edge facing upward in a custom metal clamp.

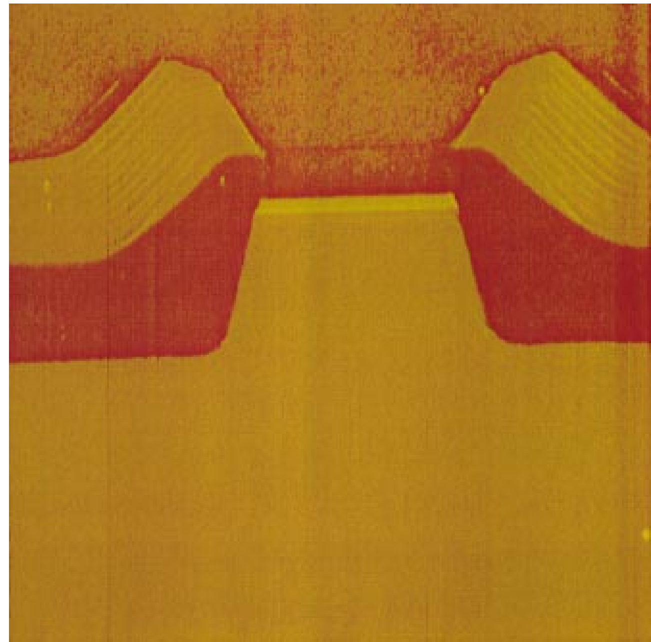

FIG. 1. SSRM image of buried heterostructure MQW laser in cross section. Tip bias was 0.5 V and the scan rate was 0.25 Hz. MQW active region (bright, narrow bar near the center of the image) is clad by *p*-doped (top) and *n*-doped (bottom) material. The image is approximately 5×5 μm.

III. RESULTS AND DISCUSSIONS

A. SSRM

Scanning spreading resistance microscopy was used to examine the cross section of the BH MQW laser structure. Figure 1 shows a typical SSRM current image obtained on the uncoated facet of the laser device. The bias voltage was 0.5 V and the tip scan rate was 0.25 Hz. The n^+ substrate is the bright band at the bottom. The buried mesa structure is clearly resolved in the SSRM image. The narrow, bright strip around the center of the image is the MQW active region, which is clad by *p*- and *n*-doped layers above and below it. Individual quantum well/barrier periods could be resolved by slowing down the SSRM scan. At the left and right sides of the active region are the symmetric $p-n-p-n$ current-blocking structures. The topographic AFM image of the BH laser, obtained simultaneously with the SSRM data, showed

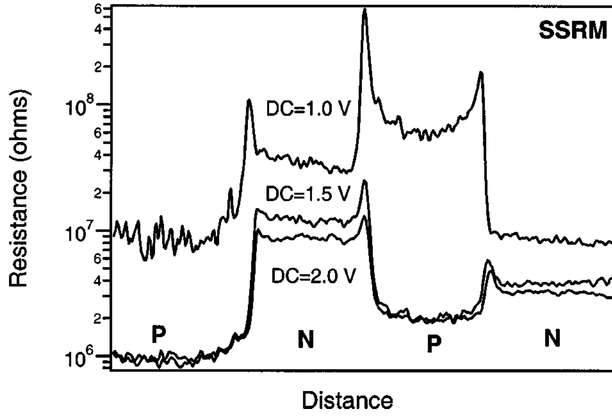

FIG. 2. Resistance profile measured by SSRM across the $p-n-p-n$ current-blocking structure of a BH laser for dc bias voltages of 1.0, 1.5, and 2.0 V. The depletion regions between *pn* junctions exhibit higher resistance at all bias voltages.

no perceptible features. Since we neglect any dependence of tip-to-sample contact resistance on tip position, the measured current is expected to be proportional to $n\mu$, the product of local carrier concentration and the mobility.

The SSRM image may be compared with the known nominal doping levels of the $p-n-p-n$ thyristor structure of the BH laser. The first layer (p doped) at the top has a higher doping concentration than the third layer (also p doped), and therefore is brighter in color (higher current under the same dc bias voltage). Similar color contrast can be observed between the second (n-type, lower doping concentration) and the fourth (n-type substrate, higher doping concentration) layers.

Figure 2 shows the averaged spreading resistance as a function of depth below the device surface in the $p-n-p-n$ structure region. The SSRM resistance profile was measured at three dc bias voltages. The resistance of every region decreases as the dc bias increases from 1.0 to 2.0 V in 0.5 V increments, indicating a bias dependence of the SSRM resistance. The effect may be attributable to the establishment of a Schottky-like contact between the probe tip and sample surface.[10]

SSRM results also shed light on the characteristics of the depletion region formed at *pn* junctions. The depletion regions are expected to have a lower conductivity, resulting in the peaks in the SSRM resistance profiles of Fig. 2. The expected width of the depletion region is approximated by

$$W=\left[\frac{2\varepsilon_r\varepsilon_0 kT}{q^2}\ln\left(\frac{N_a N_d}{n_i^2}\right)\left(\frac{1}{N_a}+\frac{1}{N_d}\right)\right]^{1/2}, \quad (1)$$

where ε_r equals to 12.56 for InP, ε_0 is permittivity of free space, q is the electronic charge, k is Boltzmann's constant, T is the temperature, and n_i is the intrinsic carrier concentration. For InP at 300 K, $n_i=1.2\times10^8$ cm^{-3}. N_a and N_d are the donor and acceptor concentrations of the materials making up the *pn* junction. The depletion region width at the *pn* junction between the second and third layers from the top of Fig. 2, is 0.07 μm. This result agrees well with the calculated value $W=0.066$ μm using the known nominal doping concentrations $N_d=1\times10^{18}$ cm^{-3} and $N_a=6\times10^{17}$ cm^{-3}.

TABLE I. SSRM resistance across the $p-n-p-n$ current-blocking layers at different dc bias voltages.

Dc bias	1.0 (V)	1.5 (V)	2.0 (V)
1st layer (p-doped)	8.56×10^6 Ω	9.84×10^5 Ω	9.22×10^5 Ω
2nd layer (n-doped)	3.55×10^7 Ω	1.23×10^7 Ω	8.77×10^6 Ω
3rd layer (p-doped)	6.06×10^7 Ω	2.05×10^6 Ω	1.94×10^6 Ω
4th layer (n-doped)	8.51×10^6 Ω	3.80×10^6 Ω	3.24×10^6 Ω

Table I shows the averaged SSRM resistance at each blocking layer of the $p-n-p-n$ structure, taken from the mean value of the resistance curve in each corresponding region of Fig. 2. The measured resistance ranges from 1×10^6 to 6×10^7 Ω, depending on the dc bias voltage and the doping concentration. These values, combined with the calibration curves discussed below, were used to derive the doping concentration of each doped layer in the $p-n-p-n$ structure.

SSRM measurements were also taken for the n- and p-type InP samples with staircase doping profile structures using the identical diamond tip, contact force, and bias voltages. We have shown that SSRM measurements of the calibration samples and the unknown structures must be carried out under identical experimental conditions to achieve quantitative agreement with SIMS.[18] The calibration curves, under dc bias voltages of 1.0, 1.5, and 2.0 V, are shown in Figs. 3(a) and 3(b). The SSRM measured resistance is plotted against the dopant concentration as determined by SIMS for (a) n-type and (b) p-type InP standards. These curves were used to obtain the carrier concentrations in $p-n-p-n$ layers of the BH laser, as will be discussed in Sec. III C.

For both n- and p-type InP standard samples, the three calibration curves obtained at three dc bias voltages from SSRM measurements converged as the doping concentration rose above 2×10^{18} cm^{-3}. The bias dependence of SSRM resistance is much more significant at low doping concentration levels (2×10^{16}–2×10^{18} cm^{-3}) than that at high doping levels (above 2×10^{18} cm^{-3}). The contact resistance between the probe tip and the sample surface clearly plays a larger role when the free-carrier concentration is lower.[10] The curves also show that the range of the dopant levels over which SSRM is operational depends on both dc bias and material doping type, but typically in a range about 10^{17}–10^{19} cm^{-3}.

Figure 4(a) shows a high-resolution SSRM image of the MQW active region of the BH laser. Shown in the inset is a transmission electron microscope image of the quantum-well region. The tip bias was 0.5 V and the scan rate was 0.25 Hz. Individual quantum wells and barriers are resolved in the

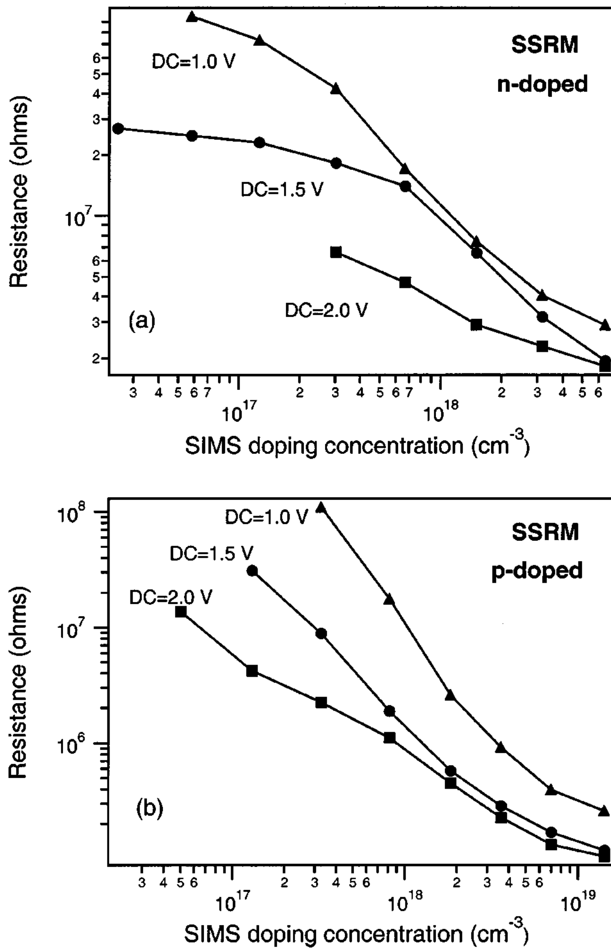

FIG. 3. SSRM resistance vs SIMS dopant concentration for Si-doped (a) and Be-doped (b) InP expitaxial layers separated by undoped InP and grown by MBE on an n^+-InP substrate. Calibration measurements were performed at three dc bias voltages: 1.0, 1.5, and 2.0 V.

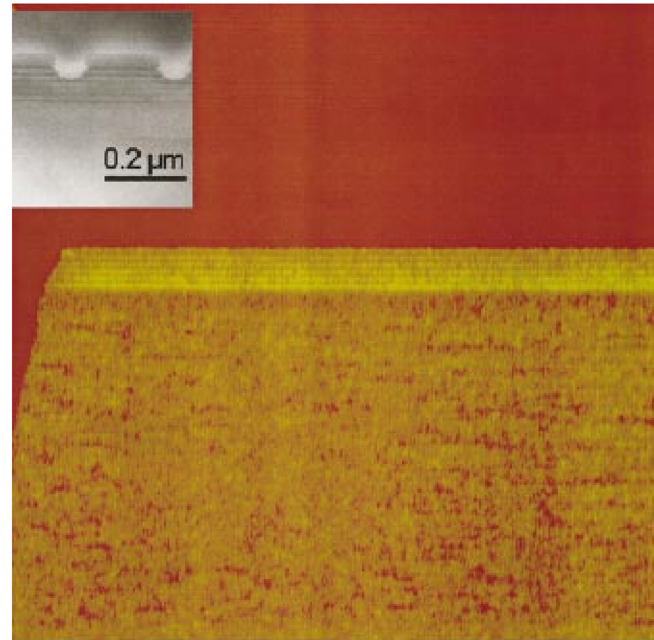

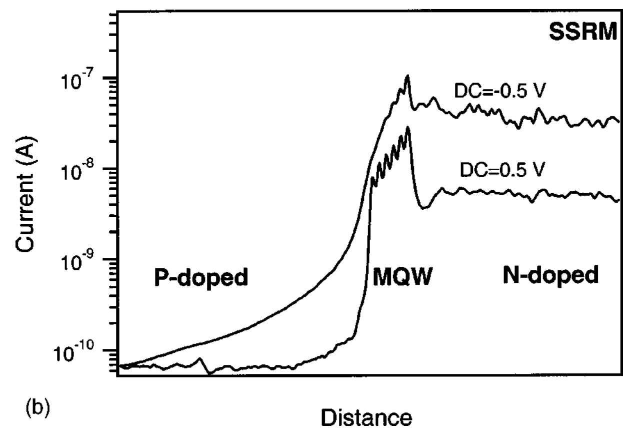

FIG. 4. (a) High-resolution SSRM image showing the quantum well structure in the active region of the BH laser. A single quantum-well–barrier period is resolved. The tip bias was 0.5 V and the scan rate was 0.25 Hz. A transmission electron microscope image of the quantum-well region is also shown in the inset. The image is approximately $1.5\times1.5\ \mu$m. (b) Cross-sectional SSRM current at dc bias voltages of 0.5 and −0.5 V throughout the MQW region.

SSRM image. The intrinsic active quantum-well region of the device appears to be brighter than both the n-doped region (below) and p-doped region (above). This effect was previously[18] attributed to the smaller band gap, higher intrinsic carrier concentration, and higher carrier mobility of the InGaAsP quantum wells that make up the active region.

In Fig. 4(b) we plot the SSRM current, measured at a dc bias voltage of 0.5 V as a function of depth below the device surface, by averaging the line scans that make up Fig. 4(a). Also shown is the current obtained at a reverse bias voltage of −0.5 V. Strong contrast in SSRM current among quantum wells and barrier layers is obtained only at forward dc bias voltage (0.5 V), confirming a strong nonlinear dependence of the SSRM current on the sample bias. An upward slope in the SSRM current in the active region can be observed in both curves. This behavior may be a consequence of the potential drop in the MQW active region (up to around 1 V) due to the built-in electrical field across the $p-i-n$ junction.

B. SCM

We also employed SCM to examine the BH lasers in cross section. SCM is a nondestructive technique in view of the weak force applied by the probe tip to the sample surface. Figure 5 shows typical SCM images obtained on the uncoated facet of the BH laser device in (a) dC/dV open-loop amplitude mode and (b) feedback closed-loop amplitude mode. The ac bias voltage was 0.5 V and the scan rate was 0.25 Hz in the open-loop mode scanning. In the closed-loop mode, the capacitance feedback set point was set to 1.0 V and the scan rate was 0.25 Hz. Both SCM images show the basic cross-sectional features of the BH laser, but the spatial resolution is not as high as in the SSRM image (Fig. 1). This difference likely occurs because the spatial resolution in the SSRM image is mostly determined by the radius of the probe tip, while the spatial resolution of a SCM image depends

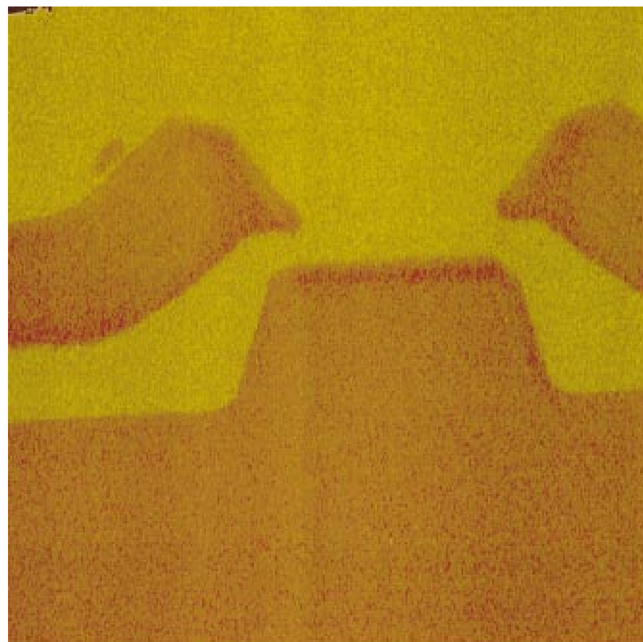

(a)

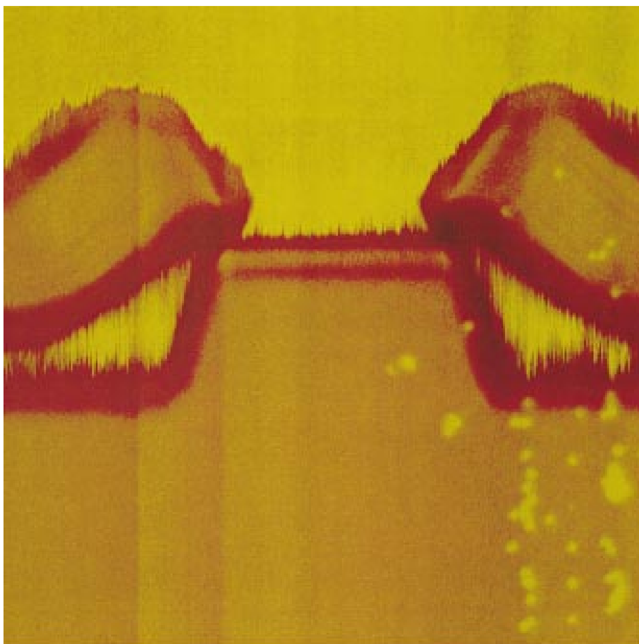

(b)

FIG. 5. Typical SCM image obtained on the cross-section of the MQW BH lasers. (a) Open-loop amplitude mode, an ac bias of 0.3 V and scan rate of 0.5 Hz; (b) closed-loop amplitude mode, a capacitance feedback set point of 1.0 V and scan rate of 0.25 Hz. The *pn* junctions are clearly delineated in both images. The images are approximately 5×5 μm.

more on the lateral distribution of the depletion region in the semiconductor underneath the probe contact point.

In the open-loop image, the *n*- and *p*-doped layers of the BH laser appear as darker and brighter regions, respectively. Due to the high image contrast between *n*- and *p*-doped regions, SCM is often used for the delineation of *pn* junctions.[19] The MQW active region looks even darker than the rest of the image, showing a more *n*-type-like behavior in the SCM response. In comparison with the SSRM image, SCM provides only a weak contrast between regions of the same doping type that have different dopant concentrations. The nonlinear correlation between the SCM signal and the carrier concentration has been discussed and reported by several groups.[17,20]

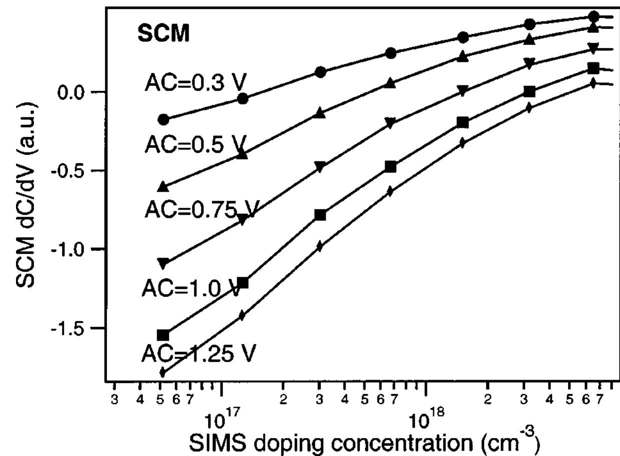

FIG. 6. SCM signal (dC/dV) vs the SIMS dopant concentration extracted from Fig. 5(a) for an *n*-type InP standard wafer. The correlation curves were obtained at each of the following ac bias voltages: 0.3, 0.5, 0.75, 1.0, and 1.25 V.

A dark broad line along the *pn* junction is observable in closed-loop images. SCM response in the closed-loop amplitude mode is much more sensitive to the junction depletion region, since the surface is already highly depleted and a small ac signal is enough to maintain the preset constant change in depletion width. The broadening of the *pn* junction, as observed in Fig. 5(b), results from the finite tip size and interaction volume.[15]

Previous investigations have sought to arrive at a straightforward correlation between the SCM signal and doping concentration in semiconductors.[21] This connection requires either that the dopant density be known at one measured position[14,15,20] or that the dopant profile and doping concentration be extracted only over a narrow range.[22] The absence of a well-established model or algorithm for direct conversion of SCM signal to doping concentration motivated us to employ standard samples with staircase doping profiles, as we did for SSRM.

Open-loop amplitude mode SCM measurements were taken for the *n*- and *p*-type InP samples with staircase doping profile structures and compared to the results of SIMS depth profile monitoring for elemental silicon (*n* dopant) and beryllium (*p* dopant). Excellent spatial correlations between the features in the SCM signal (dC/dV) and those in the SIMS data for a standard *n*-type InP sample were obtained. The SCM signal increases with rising dopant concentration over a wide dynamic range of $2 \times 10^{16} - 6 \times 10^{18}$ cm^{-3}. However, the dynamic range of the SCM signal in probing *p*-type InP material is much more restricted: as the doping concentration falls below 1×10^{17} cm^{-3} or rises above 1×10^{18} cm^{-3}, the SCM signal saturates. Stephenson and his co-workers[23] reported SCM contrast reversal in both *n*- and *p*-doped stair-

TABLE II. Comparison of doping concentration derived from calibrated SSRM and SCM measurements and SIMS nominal values for the $p-n-p-n$ current-blocking structure of the BH laser.

PNPN structure	Nominal doping density ($\times 10^{18}$)	SSRM dc=1.0 V ($\times 10^{18}$)	SSRM dc=1.5 V ($\times 10^{18}$)	SSRM dc=2.0 V ($\times 10^{18}$)	SCM ac=0.75 V ($\times 10^{18}$)	SCM ac=1.0 V ($\times 10^{18}$)	SCM ac=1.25 V ($\times 10^{18}$)
1st layer (*p*-doped)	1.0	1.2 ($\pm$20%)	1.3 ($\pm$20%)	1.0 ($\pm$20%)	⋯	⋯	⋯
2nd layer (*n*-doped)	1.0	0.37 ($\pm$20%)	0.81 ($\pm$20%)	0.15 ($\pm$20%)	0.652 ($\pm$10%)	0.902 ($\pm$10%)	0.917 ($\pm$10%)
3rd layer (*p*-doped)	0.6	0.49 ($\pm$20%)	0.79 ($\pm$20%)	0.43 ($\pm$20%)	⋯	⋯	⋯
4th layer (*n*-doped)	2.0	1.3 ($\pm$20%)	2.7 ($\pm$20%)	2.0 ($\pm$20%)	1.45 ($\pm$10%)	1.95 ($\pm$10%)	2.07 ($\pm$10%)

case structures and noted that the phenomenon is more problematic for *p*-type samples. They reported that the onset of contrast reversal may be adjusted by changing the dc sample bias, leading to a shift in the operating position of the SCM.

Five calibration curves, generated from the SCM and SIMS data on the *n*-type InP staircase structure, were measured under different ac bias voltages and are plotted in Fig. 6. The SCM signals (dC/dV) at different ac biases converge at high doping concentration levels. The dopant level over which SCM is operational is almost bias independent, i.e., around $10^{17}-10^{19}$ cm^{-3}. We now use these curves, combined with the SCM values acquired on the $p-n-p-n$ structure of the BH laser, to derive the doping concentration of the *n*-doped layers in the device.

C. Calibration results

By using the calibration curves obtained in Secs. III A and III B, the doping concentration of each layer in the $p-n-p-n$ structure of the BH laser was obtained and listed in Table II. Also provided are the nominal values of the dopant concentration in each layer. The results reveal that the SSRM-determined dopant concentration agrees with the nominal dopant density within 35%, with the exception of two values for the second layer determined from SSRM at dc=1.0 and 2.0 V. The measurement uncertainty, i.e., errors due to the random noise of the SSRM resistance or SCM signal measurements, is estimated to be 20% for SSRM and 10% for SCM, respectively. Values determined using SSRM derived from all three dc bias calibration curves for the second layer of the $p-n-p-n$ structure are all consistently lower than the corresponding nominal dopant concentration. This may be due to the confinement of the current by the *pn* junctions which surround this layer, or to the confined *n*-typed layer being particularly depleted. Other systematic errors may include the inaccuracy caused by the nonlinear behavior of the tip–sample contact.[10]

The SCM-determined dopant concentrations on *n*-doped layers exhibit reasonably consistent agreement with the nominal values. Values derived from calibration curves at ac=1.0 and 1.25 V provide less than 10% deviation from the nominal dopant density. As discussed above, calibrated SCM measurements were not possible for the *p*-type material.

IV. CONCLUSION

SSRM and SCM have been used to profile the carrier concentration in a MQW BH laser and in InP staircase structures. Good correlation between the nominal doping density and the SSRM measured dopant density was obtained for the BH lasers. SSRM imaging also resolves the depletion region at *pn* junctions, yielding a measurement of the depletion region width which agreed well with the predicted value. High-resolution SSRM imaging over the MQW active region of a BH laser yielded a sub-20 nm spatial resolution in the measured resistance. Calibration curves were obtained from SSRM and SCM measurements performed on MBE-grown InP-staircase-doped structures. SSRM measurements on *n*- and *p*-type material, and SCM measurements on *n*-type material, using the calibrated tips under appropriate sample bias conditions, showed good agreement with the nominal dopant concentration.

ACKNOWLEDGMENTS

The authors would like to thank Iain Calder, Gerry Smith, and Tae Lee at Nortel Networks; Ryan Lu and Karen Kavanagh at SFU; and Matthew Lefevre at DI for valuable discussions and technical help.

[1]J. J. Coleman, R. M. Lammert, M. L. Osowski, and A. M. Jones, IEEE J. Sel. Top. Quantum Electron. **3**, 874 (1997).
[2]Z. J. Wang, S. J. Chua, Z. Y. Zhang, F. Zhou, J. Y. Zhang, X. J. Wang, W. Wang, and H. L. Zhu, Appl. Phys. Lett. **76**, 1492 (2000).
[3]Y. Yoshida, H. Watanabe, K. Shibata, A. Takemoto, and H. Higuchi, IEEE J. Quantum Electron. **35**, 1332 (1999).
[4]T. Ohtoshi and N. Chinone, Electron. Lett. **21**, 12 (1991).
[5]K. Takemasa, M. Kubota, T. Munakata, and H. Wada, IEEE Photonics Technol. Lett. **11**, 949 (1999).
[6]P. De Wolf, J. Snauwaert, L. Hellemans, T. Clarysse, W. Vandervorst, M. D'Olieslaeger, and D. Quaeyhaegens, J. Vac. Sci. Technol. A **13**, 1699 (1995).
[7]C. Shafai, D. J. Thomson, M. Simard-Normandin, G. Mattiussi, and P. J. Scanlon, Appl. Phys. Lett. **64**, 342 (1994).
[8]J. J. Kopanski, J. F. Marchiando, D. W. Berning, R. Alvis, and H. E. Smith, J. Vac. Sci. Technol. B **16**, 339 (1998).

[9]P. De Wolf, R. Stephenson, T. Trenkler, T. Clarysse, T. Hantschel, and W. Vandervorst, J. Vac. Sci. Technol. B **18**, 361 (2000).
[10]R. P. Lu, K. L. Kavanagh, St. J. Dixon-Warren, A. J. SpringThorpe, G. Hillier, D. Macquistan, and E. Griswold, J. Vac. Sci. Technol. B **19**, 1662 (2001).
[11]P. De Wolf, T. Clarysse, W. Vandervorst, J. Snauwaert, and L. Hellemans, J. Vac. Sci. Technol. B **14**, 380 (1996).
[12]J. N. Nxumalo, D. T. Shimizu, D. J. Thomson, and M. Simard-Normadin, IEEE Electron Device Lett. **18**, 71 (1997).
[13]H. Edwards, R. McGlothlin, R. San Martin, E. U. M. Gribelyuk, R. Mahaffy, C. K. Shih, R. S. List, and V. A. Ukraintsev, Appl. Phys. Lett. **72**, 698 (1998).
[14]Y. Huang, C. C. Williams, and M. A. Wendman, J. Vac. Sci. Technol. A **14**, 1168 (1996).
[15]Y. Huang, C. C. Williams, and H. Smith, J. Vac. Sci. Technol. B **14**, 433 (1996).
[16]P. De Wolf, M. Geva, C. L. Reynolds, T. Hantschel, W. Vandervorst, and R. B. Bylsma, J. Vac. Sci. Technol. A **17**, 1285 (1999).
[17]M. Hammar, E. Rodriguez Messmer, M. Luzuy, S. Anand, S. Lourdudoss, and G. Landgren, Appl. Phys. Lett. **72**, 815 (1998).
[18]St. J. Dixon-Warren, R. P. Lu, S. Ingrey, D. Macquistan, T. Bryskiewicz, G. Smith, and B. Bryskiewicz, J. Vac. Sci. Technol. B **19**, 1752 (2001).
[19]G. H. Buh, H. J. Chung, C. K. Kim, J. H. Yi, I. T. Yoon, and Y. Kuk, Appl. Phys. Lett. **77**, 106 (2000).
[20]J. F. Marchiando, J. J. Kopanski, and J. Albers, J. Vac. Sci. Technol. B **18**, 414 (2000).
[21]E.-S. Kang, J.-W. Kang, and H.-J. Hwang, J. Vac. Sci. Technol. A **18**, 1338 (2000).
[22]V. V. Zavyalov, J. S. McMurray, and C. C. Williams, J. Appl. Phys. **85**, 7774 (1999).
[23]R. Stephenson, A. Verhulst, P. De Wolf, and M. Caymax, Appl. Phys. Lett. **73**, 2597 (1998).